MBoC | ARTICLE

Loss of REP-1 in retinal pigment epithelial cells leads to impaired phagosome processing and altered lysosomal pathway function

Rita Coelho[a,#], Pedro Antas[a,#], Ana Fragoso Fonseca[a], Daniela Oliveira[a], Cláudia Carvalho[b], Margarida L. Pedro[a], Michael J. Hall[a], Ana Sofia Falcão[a], Miguel C. Seabra[a,b,*], and Mafalda Lopes-da-Silva[a,*]

[a]iNOVA4Health, NOVA Medical School Universidade NOVA de Lisboa, Lisbon, Portugal 1169; [b]Champalimaud Research, Champalimaud Foundation, Lisbon, Portugal 1169

ABSTRACT **Choroideremia (CHM) is a rare form of retinal degeneration caused by mutations in the ubiquitously expressed *CHM* gene, encoding for Rab escort-protein-1 (REP-1). REP-1 is required for the prenylation of Rab GTPase proteins, regulators of intracellular membrane traffic, yet what specific cellular pathways are affected in CHM and how this contributes to disease progression remain unclear. Using both ARPE-19 and iPSC-derived retinal-pigmented epithelium (RPE) cells, where the *CHM* gene was knocked-out using CRISPR/Cas9, we show that *CHM*$^{-}$ cells have an increased number of lysosomes. Cathepsins and BSA-Gold were correctly delivered to the lysosomes, suggesting that lysosome organelle identity and targeting machinery are largely unaffected, yet, digestion of photoreceptor outer segments (POS)-derived-phagosomes is impaired, resulting in a doubling of undigested POS-derived autofluorescent material in *CHM*$^{-}$ cells. Delayed acquisition of LAMP1 by the phagosome was observed. These findings reveal that REP-1 loss leads to subtle lysosomal pathway dysfunction, resulting in defects in phagosome targeting and/or digestion. Our data are consistent with the idea that gradual lysosomal impairment is associated with a premature aging process, characterized by the accumulation of lipofuscin toxic material and eventual RPE and photoreceptor degeneration, which likely drives the progressive vision loss observed in patients with CHM.**

SIGNIFICANCE STATEMENT

- CHM is a disease of membrane traffic but its pathogenesis leading to retinal degeneration remains unclear.
- The authors show that REP-1 deficiency in RPE cells leads to lysosomal dysfunction, contributing to impaired POS digestion and the accumulation of undigested autofluorescent material.
- These findings suggest that subtle alterations in the lysosomal pathway in CHM may contribute to a long-term, aging-related phenotype, potentially explaining progressive retinal degeneration.

Monitoring Editor
Sergio Grinstein
Hospital for Sick Children

Received: Nov 13, 2024
Revised: Jul 17, 2025
Accepted: Jul 28, 2025

INTRODUCTION

Choroideremia (CHM) is a rare monogenic X-linked form of retinal degeneration caused by mutations in the ubiquitously expressed *CHM* gene, which encodes for Rab escort-protein-1 (REP-1). Male patients with CHM begin experiencing vision symptoms in the first decade of life, including nyctalopia (night blindness), followed by a gradual loss in peripheral vision and reaching complete blindness in late adulthood. The product of the *CHM* gene, REP-1, is required for the prenylation of Rab GTPase proteins, central regulators of intracellular membrane traffic as well as other basic cellular functions (Seabra *et al.*, 1993; 1995; Pereira-Leal *et al.*, 2001).

The loss of REP-1 can be compensated in most of the body by the ubiquitously expressed isoform REP-2 (encoded by *CHM*-like gene, *CHML*) (Cremers *et al.*, 1992; Tolmachova *et al.*, 2006; 2010; Sarkar and Moosajee, 2022). However, in the retina, the absence of REP-1 leads to slow-onset retinal degeneration starting in the periphery of the eye. We have previously shown that some critical key Rabs have a lower affinity for REP-2 in the retina (Seabra *et al.*, 1995; Seabra, 1996; Larijani *et al.*, 2003), resulting in an accumulation of unprenylated Rabs in various layers of the eye, including the choroid, the retinal-pigmented epithelium (RPE) and photoreceptors (Cremers *et al.*, 1994; Tolmachova *et al.*, 2006; Gordiyenko *et al.*, 2010). Although the REP-1 defect is apparent in most cells and tissues studied (Tolmachova *et al.*, 2006; Gordiyenko *et al.*, 2010), these defects are subclinical such that patients with CHM exhibit only retinal disease. In a mouse model, the defects caused by the loss of REP-1, specifically in the RPE, are more akin to aging, that is, a generalized defect in many trafficking pathways and accumulation of aging signs, rather than the result of a defect in a single or a few Rab GTPases (Wavre-Shapton *et al.*, 2013). In zebrafish there is no equivalent CHML gene, and mutations in CHM are lethal (Moosajee *et al.*, 2009).

Many questions remain regarding the molecular and cellular mechanisms of disease progression in CHM. Studies so far show that CHM cell phenotypes in vitro are subtle and often variable (unpublished observations). Therefore, there is a pressing need for reliable humanized in vitro cellular models where REP-1 is fully depleted. We have recently described new human-induced pluripotent stem cell–derived (iPSC) RPE CHM models, with isogenic controls, where the *CHM* gene was knocked-out using CRISPR/Cas9 (Fonseca *et al.*, 2024). Using a similar model, Raeker and colleagues show that Rab12 is significantly underprenylated in CHM$^{-/-}$ cells, leading to increased mTORC1 signaling and reduced autophagic flux (Raeker *et al.*, 2024). Interestingly, other Rabs that were significantly underprenylated included multiple Rabs involved in the endo-lysosome and secretory pathways, pointing toward the critical importance of these pathways in CHM disease progression. This study by Raeker *et al.* also confirms previous results using mouse embryonic fibroblasts, where Rab12 is the most underprenylated Rab in CHM (Storck *et al.*, 2019).

One of the main functions of the RPE is the daily phagocytosis of shed photoreceptor outer segments (POS), a complex process in which Rabs are critical players. Impaired POS degradation has been shown in human fetal RPE cells (Gordiyenko *et al.*, 2010), CHM patient–derived iPSC-RPE (Duong *et al.*, 2018), mice (Wavre-Shapton *et al.*, 2013) and zebrafish (Krock *et al.*, 2007) CHM models. *CHM* patient–derived fibroblasts and monocytes also showed delays in phagocytosis and lysosomal degradation (Strunnikova *et al.*, 2009). A recent study showed that *CHM*$^{-}$ patient fibroblasts have increased levels of endoplasmic reticulum stress and oxidative stress when compared with fibroblasts from an age-matched control donor (Sarkar *et al.*, 2023). Given the role of Rab GTPases in membrane traffic and the reported defects in POS degradation by RPE cells, it is not surprising that this continuous accumulation of undigested material can result in cell stress and eventually retinal degeneration.

The lack of robust models and adequate controls has hindered progress discovering new cell biological pathways affected by the absence of REP-1. Although there is some evidence that suggests that there are differences in immunomodulation of inflammatory factors in CHM cells, different cell models show conflicting results. Although a pool of CHM patient-derived fibroblasts showed that the levels of secreted monocyte chemotactic protein were decreased when compared with a pool of control donor-derived cells (Strunnikova *et al.*, 2009), others have shown the opposite trend using siRNA-treated human fetal RPE (Gordiyenko *et al.*, 2010). In this study, we use two newly described CHM RPE cell models; iPSC-derived human RPE and ARPE-19 cell line, to analyze in detail various steps along the endocytic, phagocytic, and lysosome pathways.

RESULTS

REP-1–deficient cells have increased numbers of lysosomal structures

To study the role of REP-1 in the lysosome pathway of RPE cells, we developed a new cellular model system where the human immortalized RPE cell line (ARPE-19) was used and the *CHM* gene was knocked-out using CRISPR/Cas9 (hereby named *CHM*$^{-}$ cells). Western blotting confirmed that this new *CHM*$^{-}$ cell line had no detectable REP-1 (Figure 1A; Supplemental Figure S2) and had a slight but consistent increase in the levels of REP-2. Moreover, in vitro prenylation assays revealed a significant increase in the overall levels of unprenylated Rabs (Figure 1A).

When structures of the lysosome pathway were analyzed in detail by immunofluorescence, ARPE-19 *CHM*$^{-}$ cells showed no difference in the morphology and number of early endosomes stained with an early endosome–associated protein 1 (EEA1) antibody (Figure 1, B and C), yet showed increased numbers of CD63 (Figure 1, B and D) and LAMP1-stained vesicles when compared with control cells (Figure 1, B and E). The mean particle size of

This article was published online ahead of print in MBoC in Press (http://www.molbiolcell.org/cgi/doi/10.1091/mbc.E24-11-0497) on August 6, 2025.

Author contributions: R.C., P.A., M.L.P., M.C.S., and M.L.S. conceived and design the experiments; R.C., P.A., A.F.F., D.O., C.C., M.L.P., M.J.H., and M.L.S. performed the experiments; R.C., P.A., A.F.F., M.C.S., and M.L.S. analyzed the data; R.C. and M.L.-D.S. prepared the digital images; M.C.S. and M.L.S. drafted the article.

Conflict of interest: The authors declare no financial conflict of interest.

[#]These authors contributed equally to this work.

*Address correspondence to: Mafalda Lopes-da-Silva (Mafalda.silva@nms.unl.pt); Miguel C. Seabra (miguel.seabra@research.fchampalimaud.org).

Abbreviations used: AFGs, autofluorescent granules; BSA, bovine serum albumin; CatD, Cathepsin D; CHM, Choroideremia; CHML, Choroideremia like gene; EEA1, Early Endosome Associated protein 1; ER, Endoplasmic Reticulum; HRP, horseradish peroxidase; iPSC, induced pluripotent stem cells; LAMP1, lysosomal associated protein 1; LAMP2, lysosomal associated protein 1; MCP-1, monocyte chemotactic protein; MEFs, mouse embryonic fibroblasts; MITF, Melanocyte Inducing Transcription Factor; mTORC1, mammalian target of rapamycin complex 1; POS, photoreceptor outer segments; REP-1, Rab escort-protein-1; REP-2, Rab escort-protein-2; RPE, Retinal Pigmented Epithelium; TEM, Transmission Electron Microscopy; TFEB, Transcription Factor EB.

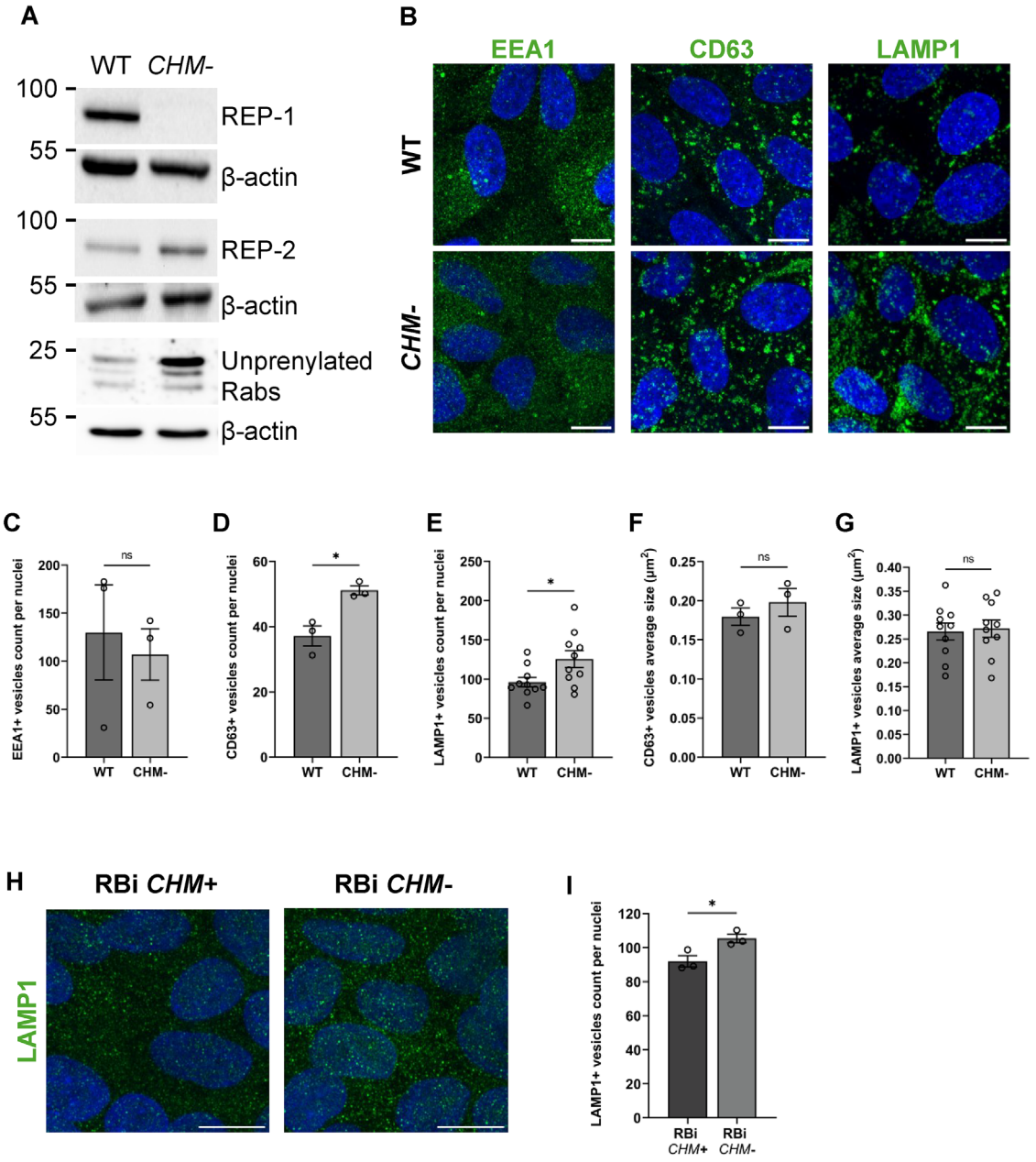

FIGURE 1: REP-1–deficient cells have increased numbers of lysosomal structures. (A) Western blot of WT and *CHM*$^{-}$ ARPE-19 cells, showing complete absence of REP-1 protein, levels of REP-2 protein and accumulation of unprenylated Rabs in *CHM*$^{-}$ cells, detected by in vitro prenylation with a biotin-labeled prenyl donor. (B) Immunofluorescence of ARPE-19 cells stained with early and late endolysosomal markers (green) with nuclei stained with DAPI (blue). (C) Quantification of the number of EEA1^{+} vesicles per nuclei in ARPE-19 cells. Data are presented as mean ± SEM, representative of $n = 3$ independent experiments. (D) Quantification of the number of CD63^{+} vesicles per nuclei in ARPE-19 cells. Data are presented as mean ± SEM, representative of $n = 3$ independent experiments. (E) Quantification of the number of LAMP1^{+} vesicles per nuclei in ARPE-19 cells. Data are presented as mean ± SEM, representative of $n = 10$ independent experiments. (F) Quantification of the average size of CD63^{+} vesicles (μm^2) in ARPE-19 cells, as measured from confocal images. Data are presented as mean ± SEM, representative of $n = 3$ independent experiments. (G) Quantification of the average size of LAMP1^{+} vesicles (μm^2) in ARPE-19 cells, as measured from confocal images. Data are presented as mean ± SEM, representative of $n = 10$ independent experiments. (H) Immunofluorescence of iPSC-RPE cells stained with LAMP1 (green) with nuclei stained with DAPI (blue). (I) Quantification of the number of LAMP1^{+} vesicles per nuclei in iPSC-RPE cells. Data are presented as mean ± SEM, representative of $n = 3$ independent experiments. All statistical comparisons were performed using unpaired Student's *t* test (ns, not significant; *$p < 0.05$); scale bar, 10 μm for all images shown.

CD63$^+$ and LAMP1$^+$ vesicles was not affected (Figure 1, B, F, and G). This suggests that although the earlier stages of the lysosome pathway seem unaffected, late-stage vesicles such as multivesicular bodies and lysosomes are disturbed by the loss of REP-1.

To verify these results in another human cell model, a human donor isogenic iPSC-derived RPE line was created using CRISPR/Cas9 to knockout the *CHM* gene (hereby named RBi *CHM*$^-$) (Fonseca *et al.*, 2024). The same increase in the number of LAMP1-stained vesicles was observed in iPSC-RPE RBi *CHM*$^-$ cells when compared with matched controls (Figure 1, H and I).

To investigate whether there were detectable morphological differences in these late-stage lysosome vesicles at the ultrastructural level, we performed transmission electron microscopy (TEM) of both cell models. To correctly identify lysosomes in ARPE-19, we preloaded the cells with BSA-gold particles by pulsing for 4 h and then chasing for 3 h in normal medium before fixation, to allow for BSA-gold particles to enter and aggregate inside lysosomes (Futter *et al.*, 1996; Burgoyne *et al.*, 2013). We could not detect any noticeable morphological differences in gold-loaded vesicles between control and *CHM*$^-$ cells (Figure 2A) but observed an increase in their number (Figure 2B) as observed by light microscopy.

When we analyzed control and *CHM*$^-$ iPSC-RPE cells by TEM (Figure 2C), we observed that iPSC-derived RPE cells are packed full of immature melanosomes, lysosome-like organelles that share constituents with lysosomes. Furthermore, when we measured the diameter of all lysosome-like vesicles we observed no difference in control and *CHM*$^-$ cells (Figure 2, C and D), suggesting that these vesicles are morphologically normal. Reassuringly, we observed the same increase in their number (Figure 2, C and E) as previously seen by light microscopy.

Because we observed an increase in the number of lysosome structures, we wanted to check whether this was due to an increase in the biogenesis of lysosomal pathway proteins. Real-time PCR of lysosomes constituents, such as LAMP1, Cathepsin D and Cathepsin B, as well as lysosomal-associated transcription factors such as transcription factor EB (TFEB) and melanocyte-inducing transcription factor (MITF), did not show any differences in mRNA levels between control and REP-1–deficient cells (Figure 2, F and G). No differences were also observed at the protein level of LAMP1, LAMP2, EEA1, Cathepsin D (pro and mature levels) (Supplemental Figure S2). This suggests that the increase in the number of lysosome vesicles is due to a defect in lysosome consumption/reformation and not increased biogenesis.

REP-1 loss causes increased levels of active Cathepsin D in lysosomes

Because REP-1–deficient cells have an increase in the number of lysosome structures, we proceeded to analyze their functional activity by measuring the activity levels of the most abundant lysosomal proteases, the cathepsins. First, correct targeting of Cathepsin D (CatD) to LAMP1-stained vesicles was observed in both control and *CHM*$^-$ cells (Supplemental Figure S1A). The number of antibody-stained CatD vesicles (which detects both pro and mature CatD) was not altered in *CHM*$^-$ cells when compared with controls (Figure 3, A and B). To assess active CatD vesicles only, we used SiR-lysosome, a cell permeable fluorescent probe that only fluoresces when it binds to active CatD (Albrecht *et al.*, 2020). We observed a significant increase in the number of active CatD vesicles in *CHM*$^-$ cells when compared with control cells (Figure 3, C and D). An even more pronounced increase was observed in iPSC-RPE *CHM*$^-$ cells when compared with isogenic controls (Figure 3, E and F). Importantly, no SiR-lysosome stain was observed in CatD-knockout ARPE-19 cells (Supplemental Figure S1B).

To further support these results, we quantified the total cellular levels of active CatD using a plate-based assay, where a substrate becomes fluorescent when it is cleaved by active Cathepsin D/E in cell lysates. We observed that *CHM*$^-$ cells showed increased levels of active Cathepsin D/E in their cytoplasm when compared with control cells (Figure 3G), in line with the results obtained with SiR-lysosome.

Together, this suggests that as the total amount of lysosomes is increased in *CHM*$^-$ cells, the amount of functional and the active degradative enzyme CatD also increases. Notably, this increase seems to be specific for Cathepsin D as Cathepsin B and Cathepsin L showed no changes in both ARPE-19 cells (Supplemental Figure S1, C and D) and iPSC-RPE cells (Supplemental Figure S1, E and F).

Loss of REP-1 affects targeting of degradative lysosomes for phagosome degradation

Previous studies showed that POS phagocytosis was impaired in REP-1–deficient human fetal RPE cells (Gordiyenko *et al.*, 2010). Conversely, we observed a significant increase in the number of late-stage lysosome vesicles and of active CatD in *CHM*$^-$ cells, so we wanted to investigate if their degradative power was affected and in what way. We have previously shown that feeding ARPE-19 cells with a single high dose of unlabeled porcine POS, the appearance of POS-derived undigested autofluorescent granules (AFG) (reminiscent of lipofuscin in vivo) can be observed over time (Escrevente *et al.*, 2021) (Figure 4A). Using this assay, we observed an increased number of *CHM*$^-$ cells containing undigested AFGs at 72 h postincubation, as measured by flow cytometry (Figure 4B). Immunofluorescence imaging and quantification of the number of AFGs per field-of-view (fov) confirmed this increase at both 24 and 72 h post-POS incubation (Figure 4, C and D). Importantly, this increase in AFG was not due to an increase in the amount of POS initially phagocytosed (Supplemental Figure S1G) as both control and *CHM*$^-$ cells fed 488-labebled POS had similar amounts of internalized phagosomes at 4 h.

We conclude that digestion of phagocytic POS in *CHM*$^-$ cell is defective despite increased numbers of active lysosomes. Given that REP-1 affects the membrane targeting and function of Rab GTPases, we hypothesize that phagosome maturation and fusion with lysosomes could be affected in *CHM*$^-$ cells. Thus, we analyzed the degree of colocalization between AFGs and LAMP1-stained vesicles to determine whether these degradative compartments were indeed fusing with phagosomes. We observed a slight but significant decrease in the amount of AFGs with at least one LAMP1$^+$ vesicle in its direct vicinity at 72 h (Figure 4, E and F). This decrease in colocalization was not significant in the initial hours after POS-feeding (Figure 4G) and was not observed with CD63 (Supplemental Figure S1, H and I).

DISCUSSION

Over the last decades, CHM research has largely focused on the clinical features and the development of new therapies, with less interest being awarded to the cellular and molecular dysfunctions underlying this disease, mainly due to a lack of adequate humanized cell models. In this study, we present evidence that the loss of REP-1 leads to subtle defects in the lysosome pathway that result in reduced digestive function and the accumulation of lipofuscin-like AFGs upon POS phagocytosis (Figure 5).

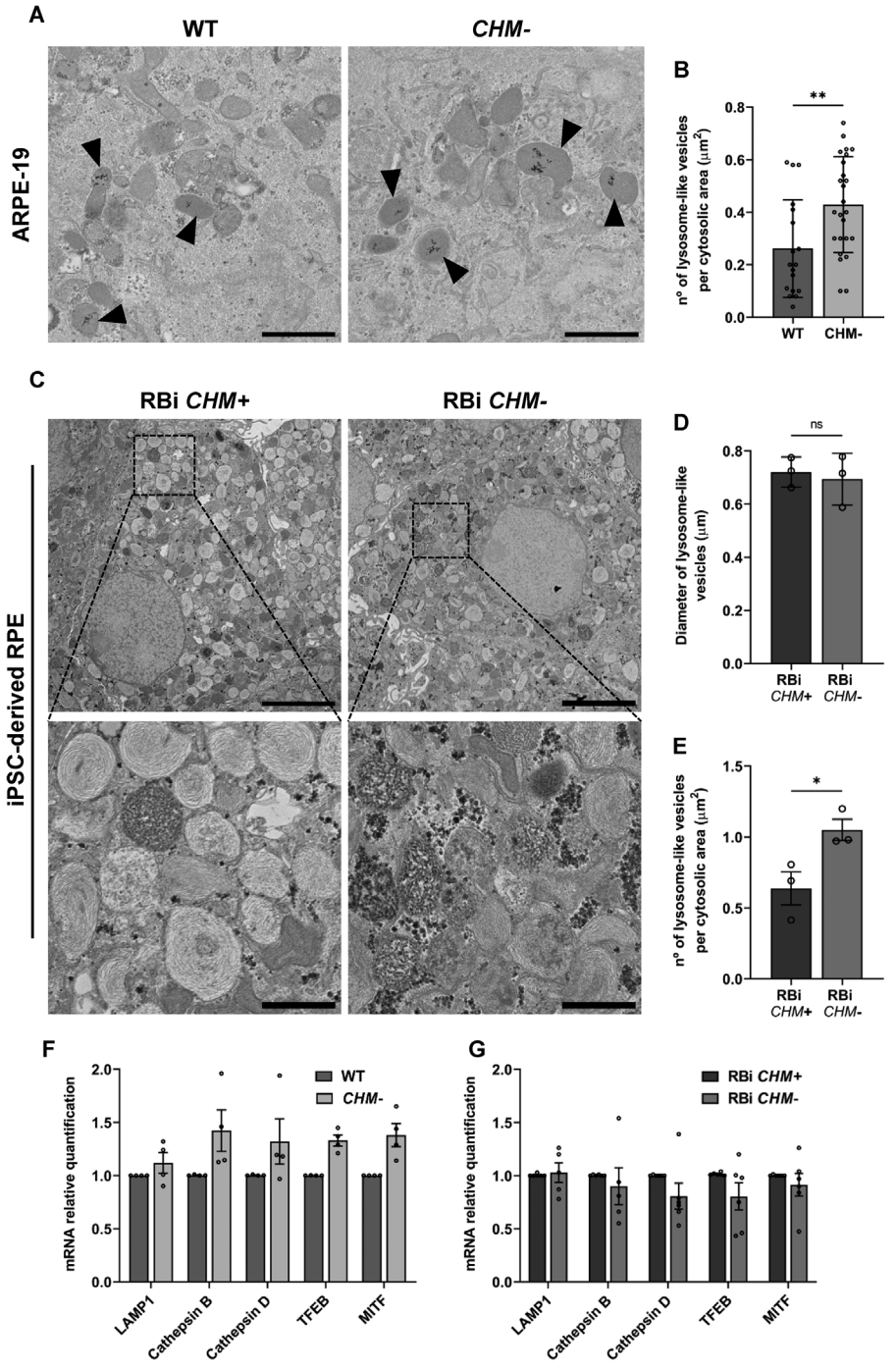

FIGURE 2: REP-1–deficient cells have morphologically normal lysosomes. (A) TEM images of ARPE-19 cells, where lysosomes have been loaded with BSA-Gold particles. Examples of lysosome-like structures are shown (arrowheads); scale bar, 1 μm. (B) Quantification of the number of lysosome-like structures in ARPE-19 cells as measured from TEM images. Data are presented as mean ± SD, representative of $n = 1$ independent experiments ($n = 79$ and $n = 185$ vesicles or $n = 18$ and $n = 25$ fov for WT and *CHM*$^{-}$ ARPE-19 cells, respectively. Statistical comparisons were performed using the unpaired Mann–Whitney test (**$p < 0.01$). (C) TEM images of control and *CHM*$^{-}$ iPSC-RPE cells showing multiple melanosome and lysosome-like structures; scale bar, 5 and 1 μm in inset images. (D) Quantification of the diameter of lysosome-like structures in iPSC-RPE cells as measured from TEM images. Data are presented as mean ± SEM, representative of $n = 3$ independent experiments. Statistical comparisons were performed using unpaired Student's *t* test (ns, not significant). (E) Quantification of the number of lysosome-like structures in iPSC-RPE cells as measured from TEM images. Data are presented as mean ± SEM, representative of $n = 3$ independent experiments. Statistical comparisons were performed using unpaired Student's *t* test (*$p < 0.05$). (F) mRNA levels of specified transcripts in ARPE-19 cells. Values for each gene are relative to WT control cells. Data are presented as mean ± SEM, representative of $n = 4$ independent experiments. No significant differences were seen. (G) mRNA levels of specified transcripts in iPSC-RPE cells. Values for each gene are relative to WT control cells. Data are presented as mean ± SEM, representative of $n = 6$ independent experiments. No significant differences were seen.

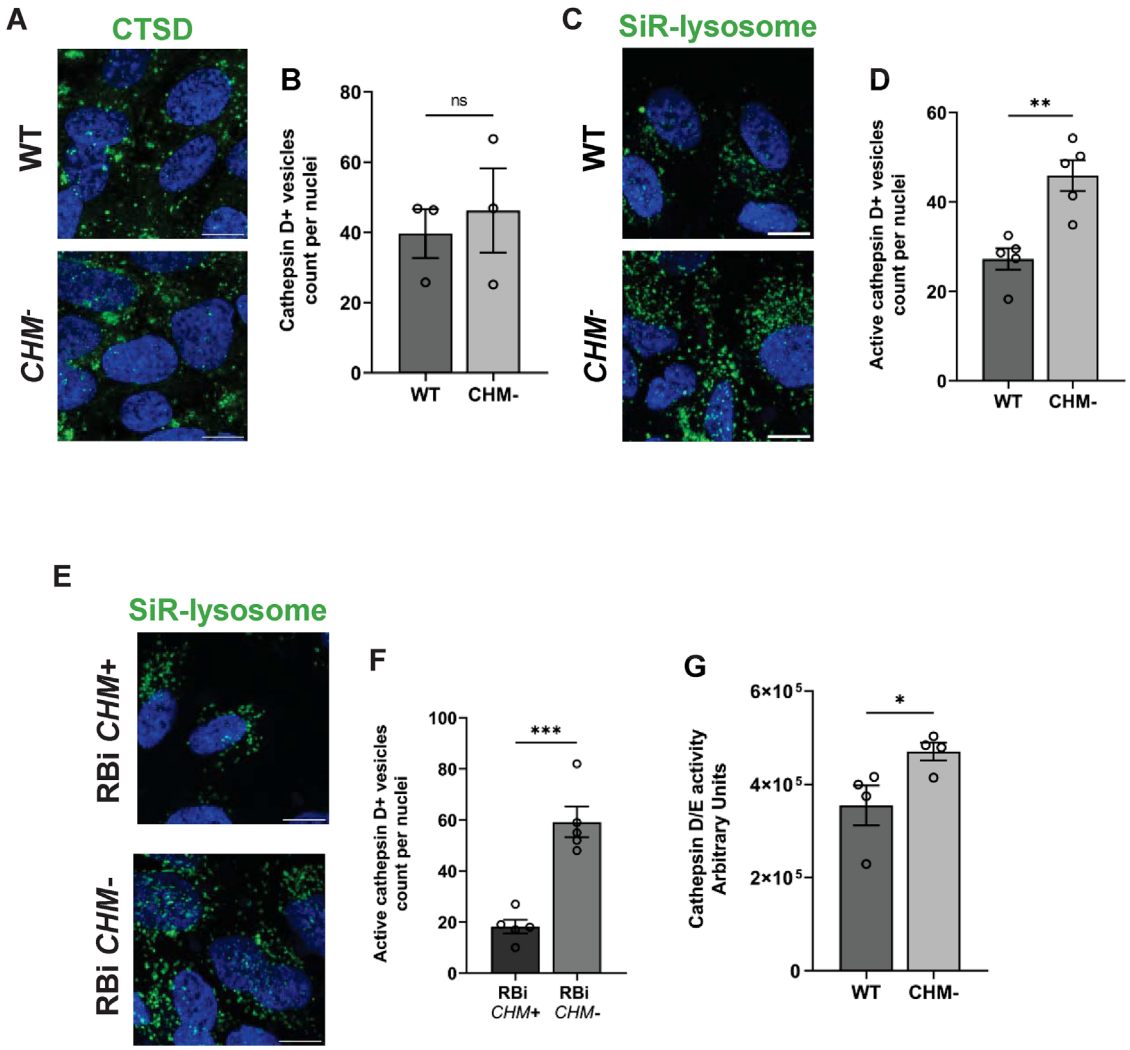

FIGURE 3: REP-1 loss causes increased levels of active Cathepsin D in lysosomes. (A) Immunofluorescence of anti-cathepsin D antibody (green)–stained vesicles with nuclei stained with DAPI (blue) in ARPE-19 cells; scale bar, 10 μm. (B) Quantification of the number of cathepsin D^+ vesicles per nuclei in ARPE-19 cells. Data are presented as mean ± SEM, representative of $n = 3$ independent experiments. Statistical comparisons were performed using the unpaired Mann–Whitney test (ns, not significant). (C) Immunofluorescence of active cathepsin D^+ (SiR-lysosome)–stained vesicles (green) with nuclei stained with DAPI (blue) in ARPE-19 cells; scale bar, 10 μm. (D) Quantification of the number of active cathepsin D^+ vesicles per nuclei in ARPE-19 cells. Data are presented as mean ± SEM, representative of $n = 5$ independent experiments. Statistical comparisons were performed using the unpaired Student's *t* test (**$p < 0.01$). (E) Immunofluorescence of active cathepsin D^+ vesicles (SiR-lysosome) marker (green) with nuclei stained with DAPI (blue) in iPSC-RPE cells; scale bar, 10 μm. (F) Quantification of the number of active cathepsin D^+ vesicles (SiR-lysosome) per nuclei in iPSC-RPE cells. Data are presented as mean ± SD, representative of $n = 1$ independent experiment ($n = 5$ fov). Statistical comparisons were performed using the unpaired Student's *t* test (***$p < 0.001$). (G) Quantification of relative units of cathepsin D/E activity in ARPE-19 cells. Data are presented as mean ± SEM, representative of $n = 4$ independent experiments. Statistical comparisons were performed using unpaired Student's *t* test (*$p < 0.05$).

The unavailability of reliable cellular models for CHM has hindered the dissection of the associated cellular defects, namely in the RPE. Here we show, wherever possible, matching results between our new ARPE-19 *CHM*$^-$ cell line and our recently described iPSC-derived RPE *CHM*$^-$ model (Fonseca *et al.*, 2024), demonstrating their utility for studying this debilitating disease. Furthermore, both models were generated using CRISPR/Cas9 editing resulting in a complete knock out of the REP-1 gene, which is what typically occurs in patients with CHM, as opposed to knockdown experiments with siRNAs that typically result in some residual protein left.

We show here that REP-1–deficient RPE cells have more lysosomes with no gross morphological defects. Also, the targeting of newly synthesized Cathepsins, including CatD, which are delivered to the lysosome via endosomes (Press *et al.*, 1998), is not affected in *CHM*$^-$ cells. Furthermore, endocytosed BSA-Gold reached lysosomes, where gold particles aggregated, providing evidence of an acidic degradative intra-lysosomal environment (Futter *et al.*, 1996), again suggesting that the lysosome pathway, including organelle identity and targeting machinery is only subtly affected in the absence of REP-1.

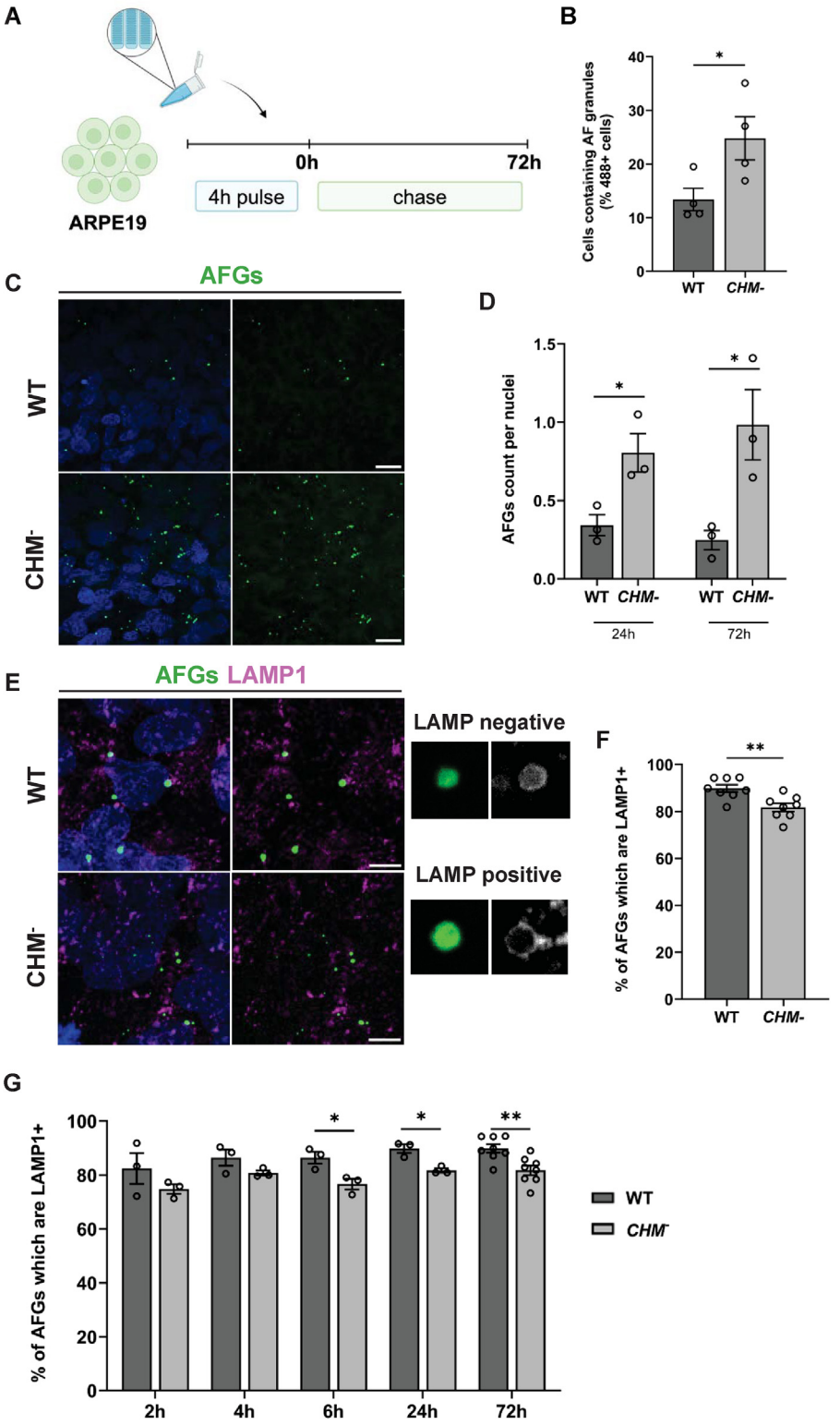

FIGURE 4: REP-1 loss effects targeting of degradative lysosomes for phagosome degradation. (A) Schematic representation of photoreceptors outer segments (POS) feeding of ARPE-19 cells. Confluent ARPE-19 cells were incubated with POS for 4 h, washed, and chased for the time points indicated (in hours). (B) Quantification of the percentage of ARPE-19 cells containing AFGs. Data are presented as mean ± SEM, representative of $n = 4$ independent experiments. Statistical comparisons were performed using unpaired Student's t test (*$p < 0.05$). (C) Immunofluorescence of AFGs (green) in ARPE-19 cells, 72 h post-POS feeding with nuclei stained with DAPI (blue); scale bar, 20 μm. (D) Quantification of the number of AFGs per nuclei at 24 and 72 h post-POS feeding in ARPE-19 cells. Data are presented as mean ± SEM, representative of $n = 3$ independent experiments. Statistical comparisons were performed using unpaired Student's t test (*$p < 0.05$). (E) Colocalization between AFGs (green) and LAMP1$^+$ vesicles

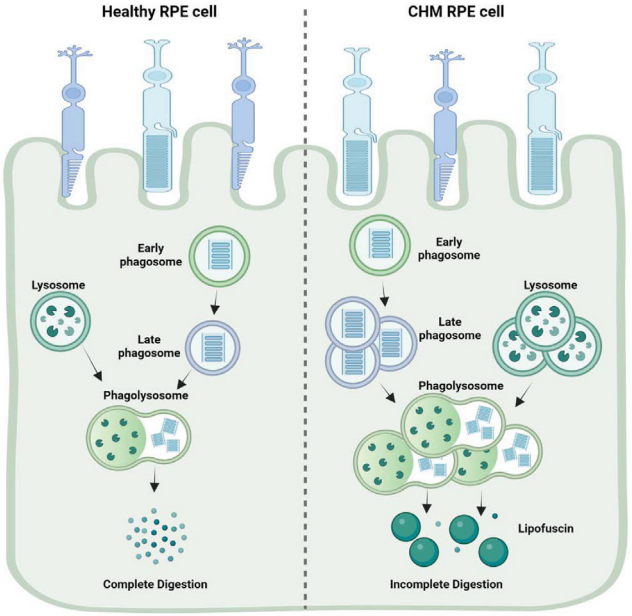

FIGURE 5: In healthy RPE cells, POS are phagocytosed by fusion of the entering phagosome with existing lysosomes. Effective and complete degradation is achieved by intralysosomal Cathepsins in the phagolysosome. In CHM-diseased RPE cells, there is increased numbers of lysosomes but nevertheless, incoming POS are not as well targeted for lysosome degradation, leading to the accumulation of undigested POS-derived material, much akin to lipofuscin in vivo.

Despite the subtle changes observed in *CHM*$^{-}$ cells, the accumulation of POS-derived AFGs was more than double that observed in control cells, as previously reported using *CHM* knockdown in human fetal RPE (Gordiyenko *et al.*, 2010). This is also consistent with observations in a mouse model, where the *Chm* gene was deleted only in the RPE, whereby phagosome maturation was delayed and the RPE-accumulated pathological changes prematurely, including the builup of lipofuscin-containing deposits as well as other age-related changes (Wavre-Shapton *et al.*, 2013).

What could explain these functional defects in vitro and in vivo? CHM is a disease characterized by a generalized partial defect in Rab GTPase activity. Furthermore, Rabs control membrane identity and fusion events between organelles of the endophagocytic system. We report here a small but significant decrease in the association of lysosome makers with incoming POS-containing phagosomes, which only decreased further with time. We suggest that this may be due to a partial defect in the targeting of lysosomes to the incoming late phagosome, and/or an inhibition of phagosome–lysosome fusion. A partial defect in Rab7 could be an attractive hypothesis, but the observation that multiple Rabs are severely underprenylated in CHM cells (Storck *et al.*, 2019; Raeker *et al.*, 2024), including Rabs associated with the endocytic system such as Rab9a, Rab12, Rab24, and Rab36, leads us to suggest that multiple Rabs are involved.

The accumulation of undigested AFGs, which in our model are a direct measure of incompletely digested POS, over time and with daily repeated POS pulses, could begin a cascade of events where undigested AFG material becomes toxic to cells, eventually leading to RPE stress and degeneration. Although we have shown that lysosome fusion with the incoming phagosome is required for AFG formation in the first place (Escrevente *et al.*, 2021), partial defects in lysosome function and/or phagolysosome fusion could explain the incomplete digestion of AFG and their increased numbers in *CHM*$^{-}$ cells. The role of melanosomes, a lysosome-related organelle filled with melanin that possesses chemiexcitation properties, in phagosome digestion, is yet to be revealed (Lyu *et al.*, 2023).

We observed no difference in the amount of mRNA of multiple lysosomal proteins (LAMP1, CathD, and CathB) as well as lysosomal transcription factors (TFEB and MITF), suggesting that the observed increase in the number of lysosomal vesicles in *CHM*$^{-}$ cells is not due to an increase in biosynthesis but instead could be a problem in the degradation/consumption of lysosomes. Another possibility could be defects in the process of lysosome reformation, which is not well understood, but surely involves multiple steps and molecular players. We have recently proposed that the drug Chloroquine acts to block lysosome fusion by interfering with lysosome reformation (Cardoso *et al.*, 2023). Chloroquine causes a gradual depletion of lysosomes with accumulation of newly synthesized procathepsin D and LAMP1, reflecting inhibition of normal turnover of lysosomal constituents. These phenotypes are clearly distinct from those observed here, and although we know that REP-1 depletion undoubtedly effects multiple steps of the lysosome pathway, we propose that the increase in the number of lysosomes observed in *CHM*$^{-}$ cells is mainly due to a fusion defect.

A recent report described the case of a 54-y-old presenting with a mild retinal degeneration initially diagnosed as a female CHM carrier (Narayan *et al.*, 2024). However, initial genetic testing did not detect a pathogenic variant and upon further testing, a novel pathogenic heterozygous variant of the *LAMP2* gene was found, confirming the diagnosis of X-linked Danon disease. The similarities in retinal phenotypes between CHM and Danon disease suggest a possible common cellular mechanism, where lysosome dysfunction plays a central role in RPE degeneration, in line with our current data. Indeed, mouse studies have shown that the lack of LAMP2 leads to defect in phagocytosis and the age-related appearance of autofluorescence abnormalities, as observed in age-related macular degeneration patients (Notomi *et al.*, 2019).

Overall, we show evidence that REP-1 deficiency does not cause gross defects in the lysosomal pathway, but instead produces subtle changes, which may only become problematic under certain (stress) conditions and/or with time (ageing). This confirms our previous suggestion that the pathogenesis of CHM is more akin to premature aging (Wavre-Shapton *et al.*, 2013). Because the RPE is responsible for the daily phagocytosis of POS, which imposes a huge and continuous phagocytic burden on these cells, these subtle alterations in the lysosomal pathway can add-up over time, and eventually cause destructive effects, such as RPE and

(magenta); scale bar, 10 μm. Examples of positive and negative colocalization are shown. (F) Quantification of the number of AFGs that colocalize with at least one LAMP1 vesicle at 72 h post-POS feeding in ARPE-19 cells. Data are presented as mean ± SEM, representative of $n = 3$ independent experiments. Statistical comparisons were performed using unpaired Student's *t* test (**$p < 0.01$). (G) Quantification of the number of AFGs that colocalize with at least one LAMP1 vesicle at the timepoints indicated post-POS feeding in ARPE-19 cells. Data are presented as mean ± SEM, representative of $n = 3$ independent experiments. Statistical comparisons were performed using unpaired Student's *t* test (*$p < 0.05$; **$p < 0.01$).

photoreceptor atrophy, contributing to vision loss in patients with CHM later in life.

MATERIALS AND METHODS

Request a protocol through *Bio-protocol*

Cell culture—ARPE-19 and iPSC

ARPE-19 cells (ATCC) were cultured in DMEM/F-12 (Life Technologies) supplemented with 10% FBS (Life Technologies) and 1% penicillin–streptomycin (Life Technologies). The production of ARPE-19 Cathepsin D-knockout cells is described in Escrevente *et al.* (2021). ARPE-19 cells were seeded at high confluency (confluent 24 h later) and were allowed to grow and polarize for at least 5 to 7 d before each assay (unless otherwise stated).

Human iPSC-derived RPE were differentiated and cultured as described in Fonseca *et al.* (2024). Gene-editing details to produce the isogenic *CHM*$^{-}$ line are also described in Fonseca *et al.* (2024). Cells were typically used for experiments around 30 d after each passage (used only during the first four passages).

ARPE-19–making CHM KO line

To generate *CHM*$^{-}$ knockout ARPE-19 cells, single-guide RNA (sgRNA) was designed for specific target regions, using the CRISPOR (http://crispor.tefor.net/) online tool and synthetically produced by Integrated DNA Technologies. CHM was targeted using the gRNA: 5′gtaaatggtgctgaagtgac3′. ARPE-19 cells were transfected following the CRISPRMAX Reagent Cas9 nuclease transfection protocol for synthetic gRNA (CMAX00001 Invitrogen) accordingly to the manufacturer's instructions. For Cas9 ribonuclease protein complex, the synthetic sgRNA was incubated with TrueCut Cas9 Protein v2 (#A36496, Invitrogen). Forty-eight hours after transfection, cells were selected by sorting as single cells and expanded for genomic DNA extraction. The targeted locus was amplified by PCR. Indel mutations were confirmed by sequencing and loss of protein by Western blot analysis.

Immunofluorescence microscopy

Cells grown on coverslips were fixed for 15 min either in 4% paraformaldehyde (Alfa Aesar) at room temperature (RT) or cold methanol on ice, according to the antibodies used. Cells were blocked/permeabilized for 30 min in PBS containing 1% BSA and 0.05% saponin for ARPE-19 cells and 1 h in PBS containing 0.05% vol/vol Triton-X100 and 10% Donkey serum for iPSC-RPE cells. Primary antibodies (1:100) were incubated with cells for 1 or 2 h at RT for ARPE-19 and iPSC-RPE, respectively. The following antibodies were used: mouse anti-LAMP1 conjugated with Alexa-fluor 647 (BioLegend, clone H4A3, Catalogue no. #328612 in 4% PFA), mouse anti-LAMP1 conjugated with Alexa-fluor 488 (BioLegend, clone H4A3, Catalogue no. #328610 in 4% PFA) rabbit anti-LAMP1 (Cell Signaling Technology, Catalogue no. #3243S in 4% PFA), mouse anti-EEA1 (BDT, Catalogue no. #610456 in 4% PFA), mouse anti-CD63 (Santa Cruz Biotechnology, Catalogue no. #sc-5275 in 4% PFA), goat anti-CTSD (SicGen, Catalogue no. #AB0043-200 in methanol). Secondary antibodies were Alexa-fluorescent conjugated (Albrecht *et al.*, 2020) and incubated at 1:500 dilution.

AFG was visualized in the 488-nm excitation wavelength. Cell nuclei were labeled with DAPI (Sigma-Aldrich, Catalogue no. #D9542-5MG) (1 µg/ml) and cells were mounted in Mowiol-mounting media (Calbiochem). Images were acquired using a Zeiss LSM980 confocal, with a Plan-Apochromat 63 × 1.4 NA oil-immersion objective. All images within the same experiment were acquired on the same day and using the same acquisition settings. Digital images were analyzed using ImageJ version 2.9.0 (https://imagej.nih.gov/ij/).

SiR-lysosome (Albrecht *et al.*, 2020) (Spirochrome, Catalogue no. #251SC012-5) staining was performed at a final concentration of 1 µM for 20 min or 1 h at 37°C for ARPE-19 and iPSC-RPE, respectively. Cells were fixed with 4% PFA for 15 min at RT, washed with PBS, stained with DAPI, and immediately mounted with Mowiol (Calbiochem) and imaged within 2 to 3 d.

IF quantifications

AFGs were automatically segmented and quantified using an ImageJ macro, which automatically identifies and segments each structure, implementing the use of automatic or manual thresholding, separation of closely joined vesicles and size exclusion. The number of AFGs was normalized by the number of nuclei in each fov (minimum eight fov; per independent experiment) and represented as the mean number of AFG detected per independent experiment ± SEM. The size of each AFGs was measured in µm^2 (area) and represented as the mean AFGs area per experiment ± SEM.

The count of lysosome structures was also carried out using an ImageJ macro, where each positively stained structure was automatically identified and segmented. The number of lysosome structures was normalized by the number of nuclei in each fov (minimum five fov per independent experiment) and represented as the mean number of lysosomal structures detected per independent experiment ± SEM. The size of lysosome structures was measured in µm^2 (area) for each individual structure and represented as the mean area per experiment ± SEM. Full macroscripts are available upon request.

For the colocalization of AFGs with lysosome structures, at least eight fov per independent experiment were used, wherein for each fov, a positive or negative value was attributed for each AFGs identified. Colocalization between AFGs and lysosome structures was represented as a percentage of positive AFGs relative to total AFGs per independent experiment ± SEM.

Cathepsin assays

ARPE-19 cells were trypsinized using TrypLE Express Enzyme (Life Technologies), washed with PBS, and lysed using a 50 mM sodium acetate buffer (0.1 M NaCl, 1 mM EDTA, 0.2% Triton X-100, pH 5.5) for 30 min at 4°C with shaking. Samples were centrifuged at 13,000 rpm for 10 min at 4°C. Protein concentration of the supernatant was quantified using the BCA protein assay kit (Thermo Fisher Scientific, #23227) according to the manufacturer's instructions. Ten micrograms of lysis protein were loaded onto a black-bottomed 96-well plate in the presence of 100 µL of sodium acetate buffer containing 10 µM of Cathepsin D/E substrate (Enzo Life Sciences, BML-P145-0001), 20 µM of Cathepsin B substrate (Enzo Life Sciences, BML-P137-0010) or 20 µM of Cathepsin L substrate (Bachem, 4003379). For Cathepsin D/E experiments an additional 25 µM of Leupeptin was added to samples and 25 µM of pepstatin A was used as a negative control. For Cathepsin B and L experiments, 25 µM of leupeptin were used as a negative control. Samples were incubated for 60 min at 37°C with fluorescence measured every 2 min with a plate reader (Synergy HT, ex: 360/40 nm; em: 420/27 nm).

RT-qPCR

mRNA from either iPSC-RPE or ARPE-19 was extracted using the RNeasy Mini Kit (#74104, Quiagen), according to the manufacturer's instructions. Next, 1 µg of purified mRNA was reverse

Primer	Sequence 5′–3′ Forward	Sequence 5′–3′ Reverse
ACTB	GAAGATCAAGATCATTGCTCCTC	ATCCACATCTGCTGGAAGG
LAMP1	CGTGTCACGAAGGCGTTTTCAG	CTGTTCTCGTCCAGCAGACACT
Cathepsin B	GCTTCGATGCACGGGAACAATG	CATTGGTGTGGATGCAGATCCG
Cathepsin D	GCAAACTGCTGGACATCGCTTG	GCCATAGTGGATGTCAAACGAGG
TFEB	AGCTCACAGATGCTGAGAG	TGTTGAACCTTCGTCTCCT
MITF	CGTCCTGTATGCAGATGGA	CATCAAGCCCAAGATTTCCTC

TABLE 1: Primer sequences used for RT-qPCR.

transcribed into cDNA using SuperScript II Reverse Transcriptase (#18064022, Invitrogen). Reverse transcriptase quantitative PCR (RT-qPCR) was carried out in a QuantStudio 5 system (Applied Biosystems) using PowerUp SYBR Green Master Mix (#A25742, Applied Biosystems) following the manufacturer's instructions. The primer pairs (forward/reverse) used are described in Table 1 and relative gene expression results were analyzed using the $2^{-\Delta\Delta Ct}$ method, normalized to the housekeeping gene *ACTB* levels.

TEM (+quantification)

All reagents and materials were purchased from Electron Microscopy Sciences unless otherwise stated. Cells on glass coverslips were fixed in 2% PFA, 2% glutaraldehyde in 0.1 M PB at pH 7.4 overnight at 4°C. After washing with PB, specimens were post-fixed with 1% osmium tetroxide and 1.5% potassium ferrocyanide in distilled water for 1 h on ice, and then incubated with 1% tannic acid for 30 min at RT. Specimens were subsequently dehydrated with a series of increasing ethanol concentrations (50, 70, 90, 2 × 100%) before infiltrating and embedding in Epon resin (EMbed 812). After polymerizing at 65°C overnight, resin blocks were sectioned at 60 to 70 nm using a Reichart Ultracut S ultramicrotome (Leica) and a diamond knife (Diatome), and sections collected on copper mesh grids. Sections on grids were poststained with uranyl acetate and Reynold's lead citrate and imaged using a Hitachi H-7650 TEM equipped with an AMT XR41 M digital camera.

The number of lysosome-like structures in each fov was identified and counted manually. To account for variations in the cytosolic area among fovs that could result in higher counts, the number of counted structures was normalized to the cytosolic area (μm^2) for the corresponding fov. To determine the size of the lysosome-like structures, the longest diameter (μm) of each vesicle was measured and recorded.

Preparation and loading of BSA-gold conjugate

After performing a stabilization test to determine the amount of protecting BSA (Sigma) required to stabilize a fixed volume of 5-nm gold colloid suspension (BBI Solutions), the appropriate volumes of BSA in 2 mM borax and 20 ml gold colloid suspension were combined. After gentle agitation for 5 min, the preparation was secondarily stabilized with a solution of 10% BSA in 2 mM borax to a final concentration of 1% BSA. The preparation was centrifuged at 45,000 rpm (205,250 × *g*) for 25 min and the fluid pellet containing the BSA-gold conjugate was extracted. The final fluid pellet formed from 22.5 ml of the starting gold colloid suspension was diluted 1:5 in media and fed to ARPE-19 cells for 4 h and then washed and further incubated for 3 h to allow for the loading of the entire lysosome pathway.

POS production and feeding

Porcine POS were isolated as described in Parinot *et al.* (2014) with some minor modifications (Escrevente *et al.*, 2021) and stored at −80°C. POS were covalently labeled with Alexa-Fluor 488 (Invitrogen) or used unlabeled. When thawed, POS were washed with PBS with three rounds of centrifugations at 5000 rpm, for 10 min at 4°C. After washing, POS were resuspended in 1 ml of PBS and kept at 4 °C until used (within one week, with minimum light exposure). ARPE-19 cells were incubated with POS for 4 h (pulse period) at a final concentration of 200 μg/ml (~2.6×10^5 POS particles/cm^2 or ~1×10^6 POS particles/ml) in DMEM/F-12 supplemented with 10% FBS. After this pulse, external POS were washed, and cells were cultured in normal ARPE-19 medium.

Flow cytometry

For the quantification of AFG using flow cytometry, cells were trypsinized with TrypLE Express Enzyme (Life Technologies) for 15 min at 37°C. Cells were resuspended in cold flow cytometry buffer (1% FBS and 2 mM EDTA in PBS), centrifuged at 1200 rpm for 5 min at 4°C and resuspended in flow cytometry buffer. Data acquisition was performed using a FACS CANTO II flow cytometer (BD Biosciences) using the 488 nm excitation wavelength to evaluate cellular AFG. 20,000 events were acquired per condition using BD FACSDiva software (Version 6.1.3, BD Biosciences) and gates were used to establish a threshold for positive 488 cells relative to no POS conditions. Results from independent experiments (at least three replicates), were represented as the percentage of 488-positive cells.

Western blot analysis

Cells were lysed in ice-cold cell lysis buffer (Cell Signaling Technology) supplemented with protease and phosphatase inhibitor cocktails (Thermo Fisher Scientific, #78444) for at least 20 min at −80°C. Lysates were scraped of the plates and pelleted for 10 min at 13,000 × *g* at 4°C and supernatants were kept for protein quantification using BCA the Protein Assay Kit (Thermo Fisher Scientific, #23227). Equal amounts of cellular proteins were resolved on 8% SDS–PAGE and subsequently transferred to 0.2-μm nitrocellulose membranes using the Trans-Blot Turbo Transfer System (Bio-Rad Laboratories, #1704150). Membranes were blocked using 5% non-fat dry milk in TBS (20 mM Tris, 140 mM NaCl, pH = 7.6) containing 0.1% Tween-20 (Sigma-Aldrich) (TBS-T) for 1 h at RT. REP-1 Primary antibody (SicGen, AB0123, 1500 dilution), REP-2 (SicGen, AB0132, 1:500 dilution), LAMP1 (Cell Signaling Technology, #3243S, 1:1500 dilution), LAMP2 (Santa Cruz Biotechnology, SC-18822), 1:1500 dilution), EEA1 (Cell Signaling Technology, #2411S, 1:1000 dilution), proCathepsinD (SicGen, AB0043-200, 1:100 dilution) were prepared in 5% BSA (NZYTech, #MB04603) and incubated overnight at 4°C. After washing with TBS-T, membranes were incubated with anti-goat, anti-mouse, or anti-rabbit horseradishe peroxidase (HRP)-conjugated secondary antibody (1:5000 in blocking buffer) for 1 h at RT. Antibody binding was detected using chemiluminescence ECL Prime Western Blotting Substrate (GE Healthcare, #RPN2232) and a ChemiDoc Touch Imaging System (Bio-Rad). An antibody to β-Actin (Sigma-Aldrich, #A3854, 1:25,000) or calnexin (SicGen, AB0041-20, 1:2000) was used as loading control.

In vitro prenylation assay

Prenylation assays were performed as described previously (Nguyen *et al.*, 2010), with minor modifications. Briefly, cells cultured in 12-well plates were washed three times with ice-cold PBS and scrapped into 100 µl of prenylation/lysis buffer (25 mM HEPES pH 7.2, 50 mM NaCl, 2 mM $MgCl_2$, 2 mM DTE, 20 µM GDP, 1x Protease and Phosphatase Inhibitor Cocktail). The cell suspensions were snap-frozen at −80°C for 30 min and then disrupted by passing through a 23-G syringe needle 20 times. Nuclei and cell debris were removed by centrifugation at 1500 × *g* for 5 min at 4°C. The resulting supernatants were collected and ultracentrifuged at 100,000 × *g* for 30 min at 4°C in an Optima XL-100K (Beckman Coulter) to separate cytosolic proteins. After quantification by BCA assay, 50 µg of cytosolic protein extract were subjected to an in vitro prenylation reaction with 20 µM GDP (Sigma-Aldrich #G7127), 0.5 µM recombinant Rab geranylgeranyl transferase (Jena Bioscience #PR-103), 0.5 µM recombinant His-tagged REP-1 (Jena Bioscience #PR-105), and 5 µM biotin-labeled geranyl pyrophosphate (Jena Bioscience #LI-015). The reaction mixture was incubated at 37°C for 1 h and then quenched with 6x SDS loading buffer. Samples were boiled at 90°C for 5 min, and biotin incorporation was analyzed by Western blot. Membranes were blocked with 5% dry milk in TBS-T for 1 h at RT, followed by overnight incubation at 4°C with HRP-conjugated streptavidin (1:2,500 in 5% dry milk; Jackson Immunoresearch #016-030-084) and anti–β-actin antibody (1:25,000 in PBS; Sigma-Aldrich #A3854) as a loading control. Chemiluminescence detection was performed using the ChemiDoc MP Imaging system (Bio-Rad). Three independent experiments were performed.

Statistical analysis

Statistical analysis was performed using GraphPad Prism, version 9.0.1 Software. All our results are shown as mean ± SEM unless otherwise stated. Normal distribution was analyzed using the Shapiro-Wilk test. Unpaired Student's *t* and Mann–Whitney tests were used to compare between groups if samples followed or not a normal distribution, respectively. The *p* values less than 0.05 were considered statistically significant.

ACKNOWLEDGMENTS

The authors thank the Molecular Mechanisms of Disease Laboratory, the Ocular Low-Cost Gene Therapy Laboratory, and the Degeneration and Aging Laboratory for their advice and support. The authors thank the Cell Culture facility at NOVA Medical School (NMS), the scientific and technical assistance of T. Pereira from the NMS Microscopy facility; and M.J.H for technical expertise and help with EM optimization and processing. We thank C. Andrade and the NMS Flow Cytometry Facility. We also acknowledge our local slaughterhouse (CASO-Centro de Abate de Suínos do Oeste) that generously provided porcine eyes. We thank the Electron Microscopy Facility at Instituto Gulbenkian de Ciência. The financial support was received for the research, authorship, and/or publication of this article. Research was supported by Fundação para a Ciência e Tecnologia (FCT)—Portugal (including iNOVA4Health projects UIDB/04462/2020, UIDP/04462/2020, and associated laboratory LS4FUTURE with reference LA/P/0087/2020), and by the Choroideremia Research Foundation. R.C. is funded by EXPL/MED-OUT/0599/2021 and "La Caixa Foundation" (NASCENT HR22-00569). P.A. is supported by grant EXPL/MED-OUT/0599/2021, funded by national funds from FCT/MCTES, and individual grant CEECIND/03862/2020. A.F.F. is funded by FCT PhD studentship (2022.12254.BD). A.S.F. postdoctoral contract is funded by "La Caixa Foundation" (NASCENT HR22-00569). M.L.S. is funded by the individual grant CEECIND/01536/2018.

Competing interests

The authors state that the research was conducted without any commercial or financial relationships that could be regarded as a potential conflict of interest.

Data availability

Raw data are available upon request to the corresponding authors.

REFERENCES

Albrecht LV, Tejeda-Muñoz N, De Robertis EM (2020). Protocol for probing regulated lysosomal activity and function in living cells. STAR Protoc, 1, 100132. https://doi.org/10.1016/J.XPRO.2020.100132

Burgoyne T, Jolly R, Martin-Martin B, Seabra MC, Piccirillo R, Schiaffino MV, Futter CE (2013). Expression of OA1 limits the fusion of a subset of MVBs with lysosomes—A mechanism potentially involved in the initial biogenesis of melanosomes. J Cell Sci, 126, 5143–5152. https://doi.org/10.1242/JCS.128561

Cardoso MH, Hall MJ, Burgoyne T, Fale P, Storm T, Escrevente C, Antas P, Seabra MC, Futter CE (2023). Impaired lysosome reformation in chloroquine-treated retinal pigment epithelial cells. Invest. Ophthalmol. Vis. Sci., 64, 10. https://doi.org/10.1167/IOVS.64.11.10

Cremers FPM, Armstrong SA, Seabra MC, Brown MS, Goldstein JL (1994). REP-2, a Rab escort protein encoded by the choroideremia-like gene. J Biol Chem, 269, 2111. https://doi.org/10.1016/S0021-9258(17)42142-9

Cremers FPM, Molloy CM, Van De Pol DJR, van Den Hurk JAJM, Bach I, Van Kessel AHMG, Ropers HH (1992). An autosomal homologue of the choroideremia gene colocalizes with the usher syndrome type II locus on the distal part of chromosome 1q. Hum Mol Genet, 1, 71–75. https://doi.org/10.1093/HMG/1.2.71

Duong TT, Vasireddy V, Ramachandran P, Herrera PS, Leo L, Merkel C, Bennett J, Mills JA (2018). Use of induced pluripotent stem cell models to probe the pathogenesis of Choroideremia and to develop a potential treatment. Stem Cell Res, 27, 140–150. https://doi.org/10.1016/j.scr.2018.01.009

Escrevente C, Falcão AS, Hall MJ, Lopes-Da-Silva M, Antas P, Mesquita MM, Ferreira IS, Helena Cardoso M, Oliveira D, Fradinho AC, *et al.* (2021). Formation of lipofuscin-like autofluorescent granules in the retinal pigment epithelium requires lysosome dysfunction. Invest Ophthalmol Vis Sci, 62, 39. https://doi.org/10.1167/IOVS.62.9.39

Fonseca AF, Coelho R, Lopes-Da-Silva M, Lemos L, Hall MJ, Oliveira D, Falcão AS, Tenreiro S, Seabra MC, Antas P (2024). Modeling choroideremia disease with isogenic induced pluripotent stem cells. Stem Cell Dev 33, 528–539. https://doi.org/10.1089/SCD.2024.0105

Futter CE, Pearse A, Hewlett LJ, Hopkins CR (1996). Multivesicular endosomes containing internalized EGF-EGF receptor complexes mature and then fuse directly with lysosomes. J Cell Biol, 132, 1011–1023. https://doi.org/10.1083/JCB.132.6.1011

Gordiyenko NV, Fariss RN, Zhi C, MacDonald IM (2010). Silencing of the CHM gene alters phagocytic and secretory pathways in the retinal pigment epithelium. Invest Ophthalmol Vis Sci, 51, 1143–1150. https://doi.org/10.1167/IOVS.09-4117

Krock BL, Bilotta J, Perkins BD (2007). Noncell-autonomous photoreceptor degeneration in a zebrafish model of choroideremia. Proc Natl Acad Sci USA, 104, 4600–4605. https://doi: *10.1073/pnas.0605818104*.

Larijani B, Hume AN, Tarafder AK, Seabra MC (2003). Multiple factors contribute to inefficient prenylation of Rab27a in Rab prenylation diseases. J Biol Chem, 278, 46798–46804. https://doi.org/10.1074/JBC.M307799200

Lyu Y, Tschulakow AV, Wang K, Brash DE, Schraermeyer U (2023). Chemiexcitation and melanin in photoreceptor disc turnover and prevention of macular degeneration. Proc Natl Acad Sci USA, 120, e2216935120. https://doi.org/10.1073/pnas.2216935120.

Moosajee M, Tulloch M, Baron RA, Gregory-Evans CY, Pereira-Leal JB, Seabra MC (2009). Single choroideremia gene in nonmammalian vertebrates explains early embryonic lethality of the zebrafish model of choroideremia. Invest Ophthalmol Vis Sci, 50, 3009–3016. https://doi.org/10.1167/IOVS.08-2755

Narayan A, Taylor LJ, Sperring S, Shanks M, Clouston P, MacLaren RE, Cehajic-Kapetanovic J (2024). A novel frameshift variant in LAMP2 gene mimicking choroideremia carrier retinopathy. Ophthalmic Genet, 45, 668–675. doi: 10.1080/13816810.2024.2404148.

Nguyen UTT, Wu Y, Goodall A, Alexandrov K (2010). Analysis of protein prenylation in vitro and in vivo using functionalized phosphoisoprenoids. Curr Protoc Protein Sci, Chapter 14:Unit14.3. https://doi.org/10.1002/0471140864.PS1403S62

Notomi S, Ishihara K, Efstathiou NE, Lee JJ, Hisatomi T, Tachibana T, Konstantinou EK, Ueta T, Murakami Y, Maidana DE, *et al.* (2019). Genetic LAMP2 deficiency accelerates the age-associated formation of basal laminar deposits in the retina. Proc Natl Acad Sci USA, 116, 23724–23734. https://doi.org/10.1073/pnas.1906643116

Parinot C, Rieu Q, Chatagnon J, Finnemann SC, Nandrot EF (2014). Large-scale purification of porcine or bovine photoreceptor outer segments for phagocytosis assays on retinal pigment epithelial cells. J Vis Exp 12, 52100. https://doi.org/10.3791/52100

Pereira-Leal JB, Hume AN, Seabra MC (2001). Prenylation of Rab GTPases: Molecular mechanisms and involvement in genetic disease. FEBS Lett, 498, 197–200. https://doi.org/10.1016/S0014-5793(01)02483-8

Press B, Feng Y, Hoflack B, Wandinger-Ness A (1998). Mutant Rab7 causes the accumulation of cathepsin d and cation-independent mannose 6–phosphate receptor in an early endocytic compartment. J Cell Biol, 140, 1075–1089. https://doi.org/10.1083/jcb.140.5.1075

Raeker M, Perera ND, Karoukis AJ, Chen L, Feathers KL, Ali RR, Thompson DA, Fahim AT (2024). Reduced retinal pigment epithelial autophagy due to loss of Rab12 prenylation in a human iPSC-RPE model of choroideremia. Cells, 13, 1068. https://doi.org/10.3390/CELLS13121068

Sarkar H, Lahne M, Nair N, Moosajee M (2023). Oxidative and endoplasmic reticulum stress represent novel therapeutic targets for choroideremia. Antioxidants, 12, 1694. https://doi.org/10.3390/ANTIOX12091694

Sarkar H, Moosajee M (2022). Choroideremia: Molecular mechanisms and therapies. Trends Mol Med, 28, 378. https://doi.org/10.1016/j.molmed.2022.02.011

Seabra MC (1996). New insights into the pathogenesis of choroideremia: A tale of two REPs. Ophthalmic Genet, 17, 43–46. https://doi.org/10.3109/13816819609057869

Seabra MC, Brown MS, Goldstein JL (1993). Retinal degeneration in choroideremia: Deficiency of Rab geranylgeranyl transferase. Science, 259, 377–381. https://doi.org/10.1126/SCIENCE.8380507

Seabra MC, Ho YK, Anant JS (1995). Deficient geranylgeranylation of Ram/Rab27 in choroideremia. J Biol Chem, 270, 24420–24427. https://doi.org/10.1074/jbc.270.41.24420

Storck EM, Morales-Sanfrutos J, Serwa RA, Panyain N, Lanyon-Hogg T, Tolmachova T, Ventimiglia LN, Martin-Serrano J, Seabra MC, Wojciak-Stothard B, *et al.* (2019). Dual chemical probes enable quantitative system-wide analysis of protein prenylation and prenylation dynamics. Nat Chem, 11, 552–561. https://doi.org/10.1038/S41557-019-0237-6

Strunnikova NV, Barb J, Sergeev YV, Thiagarajasubramanian A, Silvin C, Munson PJ, Macdonald IM (2009). Loss-of-function mutations in Rab escort protein 1 (REP-1) affect intracellular transport in fibroblasts and monocytes of choroideremia patients. PLoS ONE, 4, e8402. https://doi.org/10.1371/JOURNAL.PONE.0008402

Tolmachova T, Anders R, Abrink M, Bugeon L, Dallman MJ, Futter CE, Ramalho JS, Tonagel F, Tanimoto N, Seeliger MW, *et al.* (2006). Independent degeneration of photoreceptors and retinal pigment epithelium in conditional knockout mouse models of choroideremia. J Clin Invest, 116, 386. https://doi.org/10.1172/JCI26617

Tolmachova T, Wavre-Shapton ST, Barnard AR, MacLaren RE, Futter CE, Seabra MC (2010). Retinal pigment epithelium defects accelerate photoreceptor degeneration in cell type–specific knockout mouse models of choroideremia. Invest Ophthalmol Vis Sci, 51, 4913–4920. https://doi.org/10.1167/IOVS.09-4892

Wavre-Shapton ST, Tolmachova T, da Silva ML, Futter CE, Seabra MC (2013). Conditional ablation of the choroideremia gene causes age-related changes in mouse retinal pigment epithelium. PLoS ONE, 8, 1–11. https://doi.org/10.1371/journal.pone.0057769